Monthly Notices of the ROYAL ASTRONOMICAL SOCIETY

MNRAS **446,** 2744–2759 (2015) doi:10.1093/mnras/stu2289

Swirling around filaments: are large-scale structure vortices spinning up dark haloes?

C. Laigle,[1]★ C. Pichon,[1,2] S. Codis,[1] Y. Dubois,[1] D. Le Borgne,[1] D. Pogosyan,[3] J. Devriendt,[4] S. Peirani,[1] S. Prunet,[1] S. Rouberol,[1] A. Slyz[5] and T. Sousbie[1]

[1]*Institut d'Astrophysique de Paris & UPMC (UMR 7095), 98 bis boulevard Arago, F-75014 Paris, France*
[2]*Institute of Astronomy, University of Cambridge, Madingley Road, Cambridge CB3 0HA, UK*
[3]*Department of Physics, University of Alberta, 11322-89 Avenue, Edmonton, Alberta T6G 2G7, Canada*
[4]*Astrophysics, University of Oxford, Keble Road, Oxford OX1 3RH, UK*
[5]*KITP Kohn Hall-4030, University of California, Santa Barbara, CA 93106-4030, USA*

Accepted 2014 October 29. Received 2014 October 22; in original form 2013 October 13

ABSTRACT

The kinematic analysis of dark matter and hydrodynamical simulations suggests that the vorticity in large-scale structure is mostly confined to, and predominantly aligned with, their filaments, with an excess of probability of 20 per cent to have the angle between vorticity and filaments direction lower than 60° relative to random orientations. The cross-sections of these filaments are typically partitioned into four quadrants with opposite vorticity sign, arising from multiple flows, originating from neighbouring walls. The spins of haloes embedded within these filaments are consistently aligned with this vorticity for any halo mass, with a stronger alignment for the most massive structures up to an excess of probability of 165 per cent. The global geometry of the flow within the cosmic web is therefore qualitatively consistent with a spin acquisition for smaller haloes induced by this large-scale coherence, as argued in Codis et al. In effect, secondary anisotropic infall (originating from the vortex-rich filament within which these lower-mass haloes form) dominates the angular momentum budget of these haloes. The transition mass from alignment to orthogonality is related to the size of a given multi-flow region with a given polarity. This transition may be reconciled with the standard tidal torque theory if the latter is augmented so as to account for the larger scale anisotropic environment of walls and filaments.

Key words: methods: numerical – galaxies: formation – galaxies: haloes – large-scale structure of Universe.

1 INTRODUCTION

The standard paradigm of galaxy formation addresses the acquisition of spin via the so-called Tidal Torque Theory (TTT; Hoyle 1949; Peebles 1969; Doroshkevich 1970; White 1984) for which collapsing protogalaxies acquire their spin because of a misalignment between their inertia tensor and their (local) tidal tensor. There is ample evidence that for massive (quasi-linear) clusters, TTT provides a sound theoretical framework in which to describe angular momentum (AM) acquisition during the linear phase of structure formation. Conversely, lighter non-linear structures undergo significant drift within the large-scale tidal field, and move some distance away from their original Lagrangian patch (see e.g. Schaefer 2009, for a review). Over the last 10 years, numerical simulations as well as theoretical consideration (Birnboim & Dekel 2003; Katz et al. 2003; Kereš et al. 2005; Ocvirk, Pichon & Teyssier 2008) have accumulated evidence that the intricate cosmic web plays a critical role in the process of forming high-redshift galaxies. In the initial phase of galaxy formation, the condition of the intergalactic medium leads to essentially isothermal shocks. Hence cold gas follows closely the cosmic web while radiating away the thermal energy gained by the extraction of kinetic energy every time its trajectory dictates the formation of a shock.

The dynamical relevance of the anisotropy of the cosmic web for galaxy formation may have been partially underestimated given the small mass involved (in contrast to the mass in peaks). Indeed, spherical collapse and Press–Schechter theory have been quite successful at explaining the mass function of galaxies (Press & Schechter 1974). On the other hand, the morphology of galaxies, arguably a secondary feature, is controlled at high redshift by their spin (see e.g. Dubois et al. 2012) and is very likely driven by later infall of AM-rich gas. In turn, the critical ingredient must therefore be the anisotropy of such infall, driven by its dynamics within the cosmic web, which differ significantly (via the hitherto mentioned shocks) from that of the dark matter (DM), since cold flows advect the AM

★E-mail: laigle@iap.fr

they acquired as they formed during the early phase of large-scale structure (LSS) formation. A paradigm for the acquisition of disc AM via filamentary flows was recently proposed by Pichon et al. (2011) which found a closer connection between the 3D geometry and dynamics of the neighbouring cosmic web and the properties of embedded dark haloes and galaxies than originally suggested by the standard hierarchical formation paradigm (see also Prieto, Jimenez & Haiman 2013; Stewart et al. 2013). At these scales, in the surrounding asymmetric gravitational patch gas streams out from the neighbouring voids, towards their encompassing filaments where it shocks, until the cold flows are swallowed by the forming galaxy, advecting their newly acquired AM (Kimm et al. 2011; Tillson et al. 2012). While the gas is streamed out of the walls towards their surrounding filaments it winds up and forms the first generation of galaxies with a spin parallel to the filaments (Aragón-Calvo et al. 2007; Hahn et al. 2007; Paz, Stasyszyn & Padilla 2008; Zhang et al. 2009; Codis et al. 2012; Libeskind et al. 2013, see also Aubert, Pichon & Colombi 2004; Bailin & Steinmetz 2005, for earlier indication of anisotropic inflows). These authors explored the link between DM haloes' spins and the cosmic web to quantify this alignment. They detected a redshift-dependent mass transition $M_{\rm crit}$, varying with the scale (or equivalently with the hierarchical level of the cosmic structure in which the halo is embedded; see Aragón-Calvo & Forrest Yang 2014). Codis et al. (2012) interpreted the correlation in terms of large-scale cosmic flows: high-mass haloes have their spins perpendicular to the filament because they are the results of major mergers (see also Peirani, Mohayaee & de Freitas Pacheco 2004); low-mass haloes are not the products of merger and acquire their mass by accretion, which explains that their spins are parallel to the filament. Danovich et al. (2011) also studied the feeding of massive galaxies at high redshift through cosmic streams using the Horizon-MareNostrum simulation (Ocvirk et al. 2008) and found that galaxies are fed by one dominant stream with a tendency to be fed by three major streams. All these investigations suggest the existence of an additional mechanism affecting first low-mass haloes: mass accretion in an anisotropic, multi-flow environment.

Tempel, Stoica & Saar (2013) and Zhang et al. (2013) have recently found evidence of such alignment in the Sloan Digital Sky Survey (an orthogonality for S0 galaxies and a weak alignment for late-type spirals). The detailed origin of this correlation, while not strictly speaking surprising, as well as its measured dependence on mass, has not yet been fully understood. The spin of the dark halo represents, in essence, the vortical motion of the matter and as such can be expected to reflect the vorticity in the surrounding protogalactic patch of a forming halo. Indeed, to understand this trend, Libeskind et al. (2013) have argued that the local *vorticity* was more relevant than the original tidal field in setting up the direction of dark halo spins. They have explored the link between vorticity in halo environment and the origin of haloes spin and found a strong alignment between both. Vorticity tends to be perpendicular to the axis along which material is collapsing fastest. A natural tell-tale of such process would be a significant large-scale vorticity generation *in* the multiflow regions corresponding to the interior of filaments. Recently, Wang et al. (2014) revisited this description by introducing three invariants of the velocity gradient tensor and concluded that vorticity generation is highly correlated with large-scale structure before and after shell-crossing, in a way which depends on the flow morphology. Vorticity arises only after shell crossing in multi-streaming regions and requires the look inside such regions. Pioneering study of Pichon & Bernardeau (1999) theoretically demonstrated that in the simplest pancake-like multi-stream collapse the level of the vorticity generated is of the order of Hubble constant at the collapse stage at the scale of the thickness of the forming structures. While relying on these theoretical predictions, Codis et al. (2012) speculated that secondary shell-crossing could lead to the formation of vortices aligned with the forming filament. In turn, these vortices would account for the spin of these haloes. There is now indeed ample numerical evidence that the evolution of galaxy morphology is likely to be in part driven by the geometry of the cosmic web, and in particular its vorticity content.

Hence our focus will be in revisiting these findings with an emphasis on *where* (tracing the filaments) and *why* (studying the origin of the vorticity and its orientation) these trends are detected. We will also tentatively explain the origin of the mass transition for halo–spin alignment with the LSS's filaments. This paper aims at revisiting early stages of AM acquisition corresponding to when the cold gas/DM is expelled from neighbouring voids and walls. The main question addressed in this work will be: are there statistical evidence that swirling filaments are responsible for spinning up dark haloes and gaseous discs?

The focus will be specifically exclusively on lower mass haloes ($\rm M_{\odot} < 5\,10^{12}$) for which secondary anisotropic infall (originating from the vortex-rich filament within which they form) dominates their AM budget. To that end, we will in particular make use of filament and wall tracers in order to quantify the cosmic web, which is the natural metric for galactic evolution. The virtual data used will be DM and hydrodynamical simulations.

This paper is organized as follows. Section 2 describes the simulations and the estimators implemented in this paper. Section 3 sums up robust statistical results of (i) the orientation of the vorticity relative to the filaments, (ii) the distribution of the vorticity inside the filament and (iii) the alignment of the spin of dark haloes with the vorticity. Section 4 explores qualitatively the origin of this vorticity and uses the link between vorticity and spin to explain the non-monotonic behaviour of spin–filament alignment for haloes with masses lower than $M_{\rm crit}$. Section 5 wraps up and discusses implications. Appendix A finds consistency in alignment with the vorticity of adiabatic/cooling gas. Appendix B illustrates the transition mass in the spin/filament alignment via a simple toy model for the typical vorticity within the caustic. Appendix C studies the effect of persistence and Appendix D the effect of the variation of the smoothing scale on the alignment. Appendix E analyses the orientation of the vorticity with respect to the tidal field eigendirections. Appendix F explains the cleaning of the Friend-of-Friend halo catalogue.

2 DATA SETS AND ESTIMATORS

All the statistical results of Section 3 rely on a set of DM standard Λcold dark matter (ΛCDM) simulations presented in Table 1. These simulations are characterized by the following ΛCDM cosmology: $\Omega_{\rm m} = 0.24$, $\Omega_{\Lambda} = 0.76$, $n = 0.958$, $H_0 = 73\,{\rm km\,s^{-1}\,Mpc^{-1}}$ and $\sigma_8 = 0.77$ within one standard deviation of 3 year *Wilkinson Microwave Anisotropy Probe* results (Spergel et al. 2003).

We use different box sizes: a 100 h^{-1} Mpc box with an initial mean spatial resolution of 390 h^{-1} kpc (256^3 DM particles) in order to build a statistical sample of haloes and filaments, several 50 h^{-1} Mpc boxes with a mean spatial resolution of 190 h^{-1} kpc (256^3 particles), and a 20 h^{-1} Mpc box with a mean spatial resolution of 39 h^{-1} kpc (512^3 particles). All these simulations were run with GADGET (Springel, Yoshida & White 2001), using a softening length of 1/20th of the mean inter-particle distance. We also use the Horizon-4π simulation, a 2000 h^{-1} Mpc box $\mathcal{S}_{2000}^{\rm CDM}$ with 4096^3 DM particles (Teyssier et al. 2009).

Table 1. The set of simulations used in Sections 3 and 4. The so-called ΛHDM subset corresponds to simulations, the initial condition of which have been smoothed over 2.3 h^{-1} Mpc and 0.23 h^{-1} Mpc. The simulation $\mathcal{S}_{2000}^{\rm CDM}$ corresponds to the post-processing of an HPC simulation which allowed us to identify over 34 million haloes. The velocity field, density field, initial conditions were smoothed with Gaussian filter. In this work, we consider haloes with more than 100 particles.

Name	Type	Box size h^{-1} Mpc	Resolution	$R_{\rm velocity}$ h^{-1} Mpc	$R_{\rm density}$ h^{-1} Mpc	$R_{\rm Lagrangian}$ h^{-1} Mpc	Minimum halo mass $10^{10}{\rm M}_{\odot}$
$\mathcal{S}_{100}^{\rm CDM}$	ΛCDM	100	256^3	0.39	2.3	–	44
$\mathcal{S}_{100}^{\rm HDM}$	ΛHDM	100	256^3	0.39	2.3	2.3	–
$\mathcal{S}_{50}^{\rm CDM}$	ΛCDM	50	$256^3 \times (20)$	0.78	1.2	–	6.2
$\mathcal{S}_{20}^{\rm CDM}$	ΛCDM	20	512^3	0.039	0.23	–	0.044
$\mathcal{S}_{20}^{\rm HDM}$	ΛHDM	20	512^3	0.039	0.23	0.23	–
$\mathcal{S}_{2000}^{\rm CDM}$	ΛCDM	2000	4096^3	–	5	–	77

In addition, the ΛHDM subset corresponds to simulations with initial conditions that have been smoothed with a Gaussian filtering on scales of 2.3 and 0.23 h^{-1} Mpc, respectively, to suppress small-scale modes for the purpose of visualization and interpretation. All simulations but the sets $\mathcal{S}_{50}^{\rm CDM}$, $\mathcal{S}_{2000}^{\rm CDM}$ share the same phases.

All the simulations are studied at redshift $z = 0$. DM haloes are defined thanks to the Friend-of-Friend Algorithm (or FOF; Huchra & Geller 1982), with a linking length of $0.2(L_{\rm box}^3/N_{\rm part})^{1/3}$. In the present work, we only consider haloes with more than 100 particles, which corresponds to a minimum halo mass of 62×10^{10} $\mathrm{M}_{\odot}$ in $\mathcal{S}_{50}^{\rm CDM}$. The spin of a halo is defined as the sum over its particles i: $\sum_i (\boldsymbol{r}_i - \overline{\boldsymbol{r}}) \times (\boldsymbol{v}_i - \overline{\boldsymbol{v}})$ where $\overline{\boldsymbol{r}}$ is the centre of mass of the FOF and $\overline{\boldsymbol{v}}$ its mean velocity. As discussed in Pueblas & Scoccimarro (2009), for the DM simulations we sample optimally the velocity field using a Delaunay tessellation.

The FOF is prone to spuriously link neighbouring structures with tenuous bridges of particles, leading to artificial objects with a very high velocity dispersion, which could eventually bias the measure of the spin and consequently the alignment of the spin and the vorticity. Appendix F investigates the effect of such spurious linkage on vorticity alignments and allows us to conclude that it does not impact the result.

The vorticity of the velocity is then measured from the resampled velocity at each point of the 256^3 grid as the curl of the velocity field $\boldsymbol{\omega} = \nabla \times \boldsymbol{v}$, after Gaussian smoothing of the velocity field with a kernel length of 390 h^{-1} kpc for $\mathcal{S}_{100}^{\rm CDM}$ and $\mathcal{S}_{100}^{\rm HDM}$, a kernel length of 780 h^{-1} kpc for $\mathcal{S}_{50}^{\rm CDM}$ and a kernel length of 39 h^{-1} kpc for $\mathcal{S}_{20}^{\rm CDM}$ and $\mathcal{S}_{20}^{\rm HDM}$. The effect of the smoothing scale on the statistical alignments presented below is investigated in Appendix D. The results do not qualitatively depend on the smoothing scale and the main conclusion remains unchanged, even if the magnitude of the signal varies slightly (but not monotically) according to the scale.

A comparison between vorticity maps in $\mathcal{S}_{20}^{\rm CDM}$ and in $\mathcal{S}_{20}^{\rm HDM}$ is shown in Fig. 1. Vorticity along the normal to the section is plotted in the right panels of this figure. In $\mathcal{S}_{20}^{\rm HDM}$, high frequencies features are suppressed but the low-frequency vorticity remains consistent with that of the more realistic $\mathcal{S}_{20}^{\rm CDM}$. In $\mathcal{S}_{100}^{\rm HDM}$, the smoothing is chosen such that in high-vorticity regions (defined here as being regions where the vorticity is greater than 20 per cent of the maximum vorticity), the mean vorticity is of the order of 90 h km s^{-1} Mpc^{-1}, i.e. it corresponds more or less to one revolution per Hubble time, in agreement with the theoretical predictions of Pichon & Bernardeau (1999). The orders of magnitude are similar in $\mathcal{S}_{100}^{\rm CDM}$, $\mathcal{S}_{20}^{\rm HDM}$ and $\mathcal{S}_{20}^{\rm CDM}$.

The cosmic network is identified with RSEX and DISPERSE, the filament tracing algorithms based on either watershedding (Sousbie, Colombi & Pichon 2009) or persistence (Sousbie 2011; Sousbie, Pichon & Kawahara 2011) without significant difference for the purpose of this investigation. The first method identifies ridges as the boundaries of walls which are themselves the boundaries of voids. The second one identifies them as the 'special' lines connecting topologically robust (filament-like) saddle points to peaks. In this paper, the scale at which the filaments are traced (6 pixels Gaussian for each simulation) corresponds to large enough scales so that we are investigating the flow relative to the LSS (though see Appendix C for variations). Filaments are defined as a set of small segments linking neighbours pixels together. The mean size of the segments is 0.6 pixels, which means 234 h^{-1} kpc in $\mathcal{S}_{100}^{\rm CDM}$.

For comparison with previous studies (e.g. Libeskind et al. 2013), walls are defined according to the density Hessian. Given λ_i the eigenvalues of the Hessian $\mathcal{H} = \partial^2\rho/\partial \mathrm{r}_i \partial \mathrm{r}_j$ where ρ is the density field, with $\lambda_i > \lambda_j$ if $i < j$, walls are identified as being the region of space where $\lambda_1 > \lambda_2 > 0$ and $\lambda_3 < 0$. The normal of a wall is given by the direction of the eigenvector associated with λ_3. To obtain the Hessian, the density field of $\mathcal{S}_{100}^{\rm CDM}$ is smoothed with a Gaussian filter of 1.6 h^{-1}Mpc and differentiation of the density field is performed in Fourier space.

To estimate the number of multi-flow regions within the caustic and their size, for each segment of the skeleton, the vorticity cube is cut with a plane perpendicular to the direction of the filament. The number of multi-flow regions is given by the number of regions of positive and negative projected vorticity along this direction (with a given threshold), counted in a small window centred on the filament. To obtain the size of the regions with a given polarity, the area where the absolute projected vorticity along the normal is greater than 10 per cent of the maximum vorticity is measured, and this area is divided by the number of quadrants. Assuming that these regions are quarter of discs, it yields the corresponding radius. This measure is done in $\mathcal{S}_{100}^{\rm HDM}$.

3 STATISTICAL ALIGNMENTS

Let us first present robust statistical results derived from sets of ΛCDM simulations and ΛHDM simulations for comparison.

3.1 Correlation between vorticity and filaments

The alignment of vorticity with the direction of the filaments is examined in $\mathcal{S}_{100}^{\rm CDM}$ and in $\mathcal{S}_{100}^{\rm HDM}$. The angle μ_1 between the direction

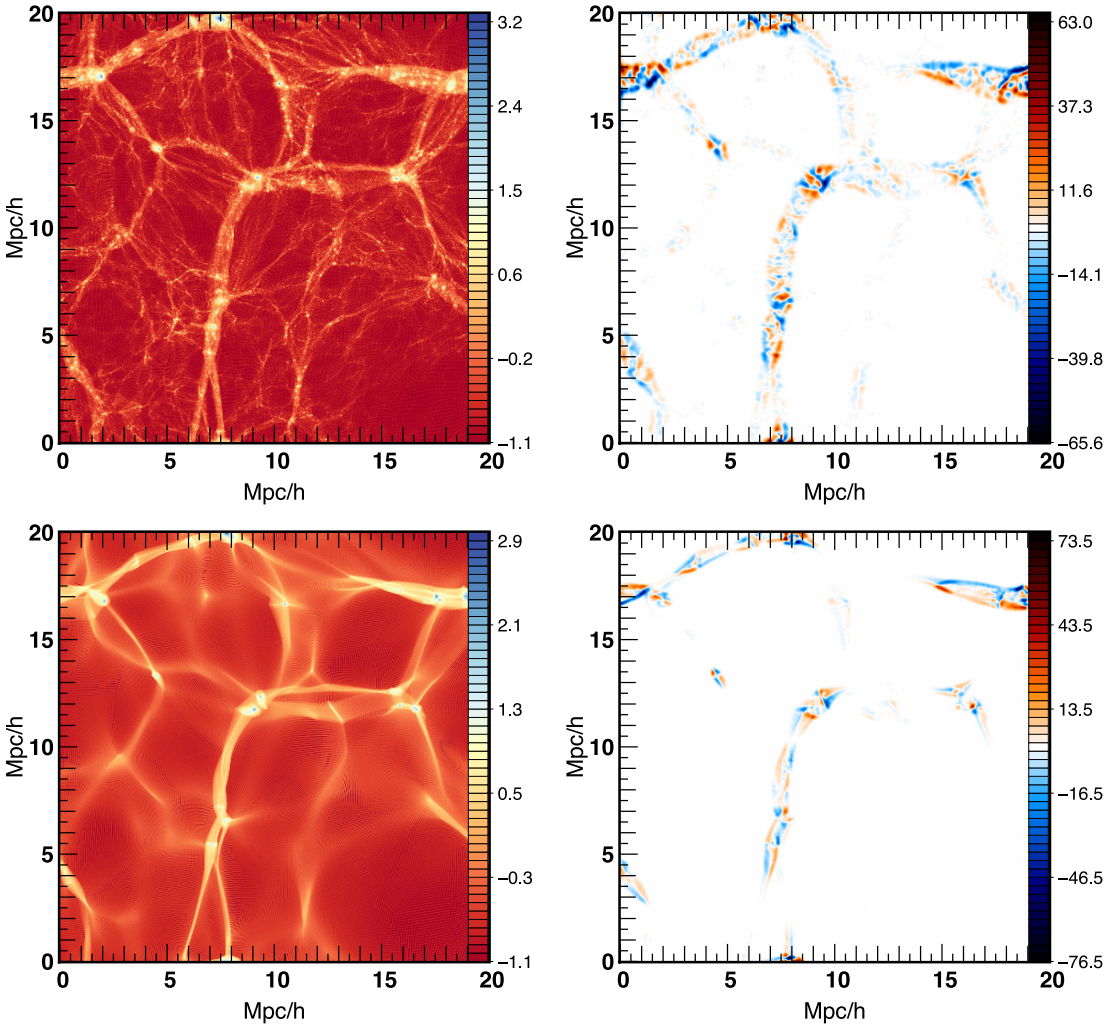

Figure 1. A thin slice ($2\,h^{-1}$ Mpc thickness) of the projected DM density (left panels) and the projected vorticity along the normal to the slice in unit of $h\,\mathrm{km\,s^{-1}\,Mpc^{-1}}$ (right panels). DM density is plotted with a logarithmic scale. Vorticity is computed after smoothing of the velocity field with a Gaussian filter of 160 h^{-1} kpc for this figure only. The geometry of the vorticity closely follows the LSS, but switches polarity across the walls/filaments (recalling that walls appear as filaments and filaments as peaks in such a cross-section). Note also how the vorticity is localized around filaments (the 2D peaks, as exemplified in Fig. 7). The two panels allow for a comparison between a section of $\mathcal{S}_{20}^{\mathrm{CDM}}$ (top) and $\mathcal{S}_{20}^{\mathrm{HDM}}$ (bottom). In $\mathcal{S}_{20}^{\mathrm{HDM}}$, high-frequency modes are suppressed but the low-frequency vorticity is qualitatively consistent with that found in the realistic $\mathcal{S}_{20}^{\mathrm{CDM}}$. On the bottom left panel, the density caustics are quite visible and correspond to the outer edge of the multi-flow region in the bottom right panel.

of the vorticity and the direction of the filament is measured along each segment of the skeleton, and μ_2 between the direction of the vorticity and the direction of the normal of the wall. The probability distribution function (PDF) of the absolute value of the cosine of these angles is shown in Fig. 2. This PDF is normalized for $\cos\mu$ between 0 and 1. A strong detection is achieved. The signal is stronger in $\mathcal{S}_{100}^{\mathrm{HDM}}$ (because of a smoothing of high frequencies) but a clear signal is also detected in $\mathcal{S}_{100}^{\mathrm{CDM}}$. As a check, the alignment between vorticity and shuffled segment directions is then measured: no signal is detected.

In the filaments we find an excess of probability of 20 per cent to have $|\cos\mu_1|$ in [0.5, 1] (that is $0 \leq \mu_1 \leq 60^\circ$) relative to random orientations. In the walls, we find an excess of probability of 45 per cent to have $|\cos\mu_2|$ in [0, 0.5] (that is $60^\circ \leq \mu_2 \leq 90^\circ$) relative to random orientations, which means a strong signal for the vorticity to be aligned with the filament, and perpendicular to the normal of the surrounding wall.

We conclude that in the neighbourhood of filaments, vorticity is preferentially aligned with the filament's axis and perpendicular to the normal of walls. In other words, vorticity tends to be perpendicular to the axis along which material is collapsing fastest. This result is consistent with that of Libeskind et al. (2013), which explored the correlation between vorticity and shear eigenvectors. This correlation is confirmed in Appendix E.

3.2 Geometry of the multi-flow region

Since Section 3.1 showed that vorticity tends to be aligned with the filamentary features of the cosmic web, we are naturally led to focus on the structure of high-vorticity regions. The kinematics of the cross-sections of the filaments is therefore examined, by cutting our simulation with a plane perpendicular to the direction of the filament. We represent in this plane the projected vorticity along the filament. Results are shown in Fig. 3 and can be summarized

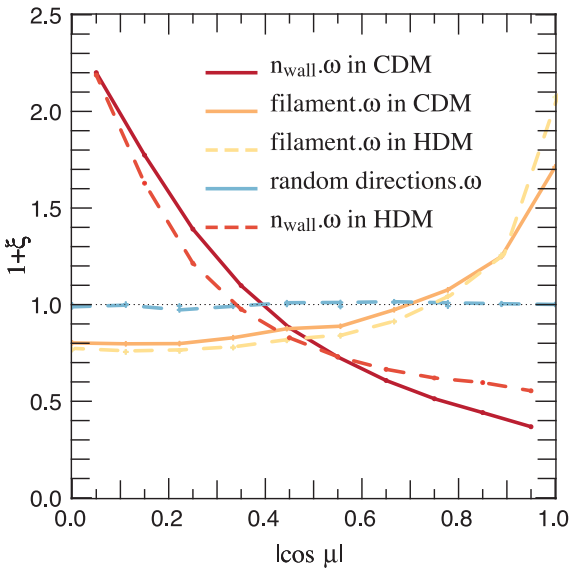

Figure 2. The PDF of $\cos\mu$, the cosine of the angle between the vorticity and the direction of the filament (orange) and the angle between the vorticity and the normal of wall (red) measured in the simulations $\mathcal{S}_{100}^{\rm CDM}$ (solid) and $\mathcal{S}_{100}^{\rm HDM}$ (dashed). The black dotted line corresponds to zero excess probability for reference. The large-scale total vorticity is preferentially aligned with filament axis.

as follows: (i) vorticity is null outside the multi-flow region, and so confined to filaments (and walls in a weaker way) which is consistent with the assumption that cosmic flows are irrotational before shell-crossing; (ii) the cross-sections of the filaments are partitioned into typically quadripolar multi-flow regions (see Fig. 4) where the vorticity is symmetric with respect to the centre of the (density) caustic such that the global vorticity within that caustic is null (as expected); the typical size of each quadrant is of the order of a smoothing scale (as shown in Fig. 4); (iii) high-vorticity resides in the low-density regions of filaments: vorticity is mainly located at the edge of the multi-flow region *on* the caustic (see also Fig. 10); vorticity is in fact typically null *at* the peak of density. (iv) Each quadrant of the multi-flow region is fed by multiple flows, originating from neighbouring walls (see Fig. 9).

3.3 Correlation between vorticity and spin

The alignment of vorticity with filaments on the one hand, and previous results about alignment (or orthogonality) of the low-mass (high-mass) haloes spin with the filament and the shear eigenvectors (Codis et al. 2012; Libeskind et al. 2012) on the other hand, suggests to revisit the alignment of spin with the vorticity (previously examined by Libeskind et al. 2012) and to analyse in depth the correlation between vorticity and AM. The measurement is done by computing the vorticity at the positions of the haloes and the projection, $\cos\theta$, between both normalized vectors. First note that haloes typically stand within one quadrant of the vorticity within filaments and not at the intersection of these quadrants, which is why the spin/vorticity alignment is strong.

The resulting PDF of $\cos\theta$ is displayed in Fig. 5. Here the set of simulations, $\mathcal{S}_{50}^{\rm CDM}$ are used to compute error bars on the correlation between spin and vorticity. The measured correlations are noisier as only a finite number of dark haloes are found within the simulation volume. It was checked that the correlation is not dominated by the intrinsic vorticity of the haloes themselves by computing the alignment between the spin and the vorticity of the field *after extruding* the FOF haloes, which led to no significant difference in the amplitude of the correlation. We find an excess probability of 25 per cent relative to random orientations to have $\cos\theta$ in [0.5, 1] for haloes with $10 \leq \log(M/{\rm M}_\odot) \leq 11$, 55 per cent for $11 \leq \log(M/{\rm M}_\odot) \leq 12$ and 165 per cent for $12 \leq \log(M/{\rm M}_\odot) \leq 13$. Note importantly that the intricate geometry of the multi-flow region (see also Figs 7 and G1) strongly suggests retrospectively that the alignment (including polarity) between the spin of DM haloes and the vorticity of the flow within that region cannot be coincidental.

Fig. 6, which presents PDF of the cosine of the angle between the spin of 43 million dark haloes and the direction of the closest filament identified in the $\mathcal{S}_{2000}^{\rm CDM}$ simulation, displays an interesting

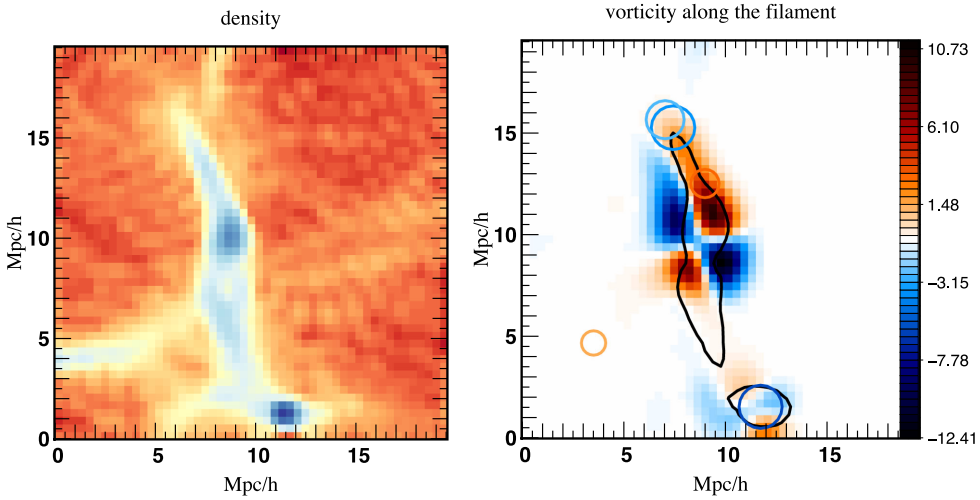

Figure 3. Geometry/kinematics of a typical multi-flow region across a filament. Left: density map of a section perpendicular to a given filament in logarithmic scale. Right: projected vorticity along the filament within that section (towards observer in red and away from the observer in blue) in units of $h\,{\rm km\,s^{-1}\,Mpc^{-1}}$ on which is plotted in dark a contour of the density. Circles are haloes with their corresponding virial radius. The colour of the circles matches to the values of $\cos\theta$ between the haloes spins and the normal of the section, positively oriented towards us. $\mathcal{S}_{100}^{\rm HDM}$ is used here, and for this figure only, vorticity is computed after smoothing the velocity field with a Gaussian filter of $1.6\,h^{-1}$ Mpc.

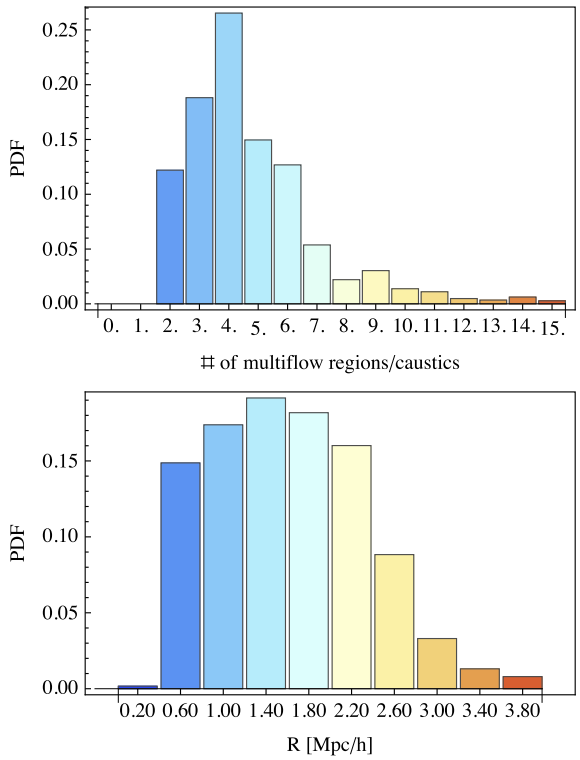

Figure 4. Top: normalized histogram of the number of multi-flow regions with different polarity around a filament measured in the simulation $\mathcal{S}_{100}^{\rm HDM}$. The mean corresponds to $\langle n_{\rm multiflow}\rangle = 4.6$, the median is 4.25. On large scales, the multi-flow region is therefore typically quadrupolar. Bottom: normalized histogram of the size of a region in $\mathcal{S}_{100}^{\rm HDM}$ with a given polarity. The mean size of such region is $\langle R\rangle = 1.6\,h^{-1}$ Mpc, somewhat below the smoothing length of the initial conditions, $R_s = 2.3\,h^{-1}$ Mpc. It was checked on $\mathcal{S}_{20}^{\rm HDM}$that a similar scaling applies.

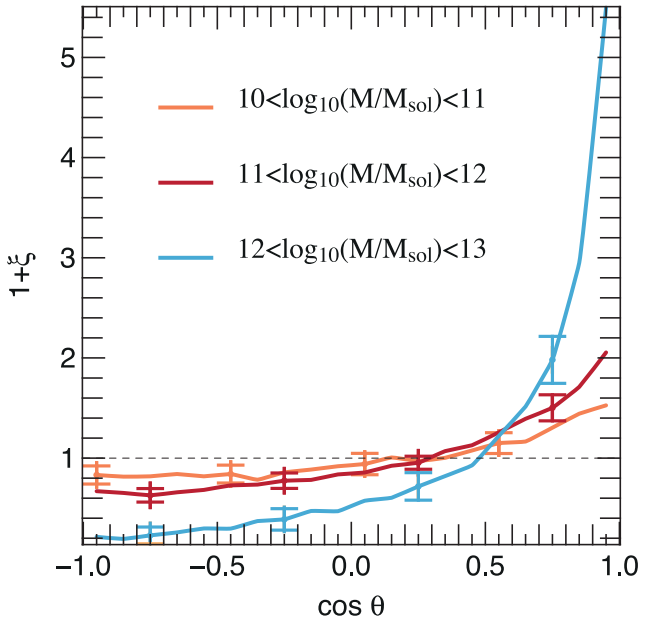

Figure 5. The PDF of the angle between the vorticity and the spin measured in 20 simulations of the $\mathcal{S}_{50}^{\rm CDM}$ set. Haloes are binned by mass as labelled. The displayed error bars are 1σ standard deviation on the mean.

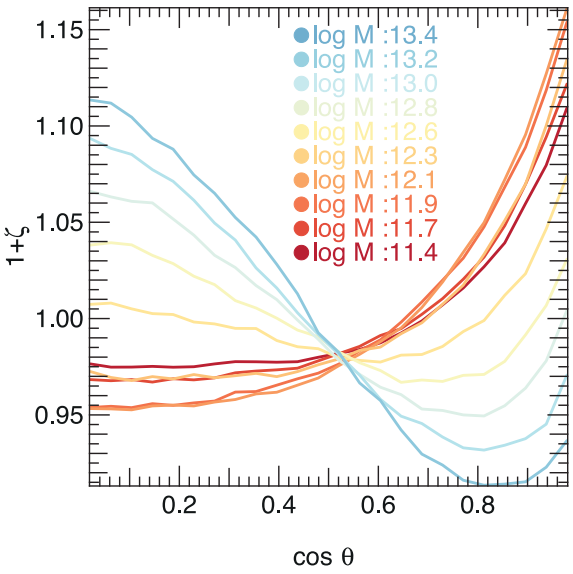

Figure 6. The probability distribution of the cosine of the angle between the spin of dark haloes and the direction of the closest filament as a function of mass in the $\mathcal{S}_{2000}^{\rm CDM}$ simulation. The smoothing length over which filaments are defined is 5 h^{-1} Mpc. This figure extends the result first reported in Codis et al. (2012) to the mass range $\log M/{\rm M}_\odot \sim 11.5$–$12.0$. In this mass range one observes that the probability to have a small angle between the halo's spin and the filament's direction first *increases* (in red) as mass grows to $\log M/{\rm M}_\odot \sim 12.1$, in agreement with the increased spin–vorticity alignment demonstrated in Fig. 5. At larger masses (from orange to blue) the statistical spin–filament alignment quickly decays, with a critical mass (in yellow) corresponding to a transition to predominately orthogonal orientations (in blue) at $\log M_{\rm crit}/{\rm M}_\odot \approx 12.7$ as defined by Codis et al. (2012).

feature at low mass. For the range of mass $\log M/{\rm M}_\odot \sim 11.5$-$12.5$, the actual alignment between the spin and the direction of the filament *increases* with mass, before it becomes abruptly perpendicular around $5 \times 10^{12}\,{\rm M}_\odot$. This is fully consistent with the corresponding increase in vorticity shown in Fig. 5, and will be discussed further in the next section.

4 INTERPRETATION

Let us now turn to the visualization of special purpose simulations, the ΛHDM set, to identify the origin and implications of the measured vorticity of Section 3, and explain the observed mass transition.

4.1 Building up vorticity from LSS flow

Let us first show that density walls are preferentially aligned with zero-vorticity walls.

Fig. 7 displays the vorticity field in the neighbourhood of the main filament of the idealized 'HDM' simulation, $\mathcal{S}_{20}^{\rm HDM}$. The vorticity bundle is clearly coherent on large scales, and aligned with the direction of the filament, strongest within its multi-flow core region, while its essentially quadrupolarity is twisted around it.

Fig. 8 displays the cross-section of the vorticity perpendicular to the main filament shown in Fig. 7. The velocity field lines (in blue) converge towards the local walls (in brown) and are visually in agreement with the vorticity field which is partitioned by these walls.

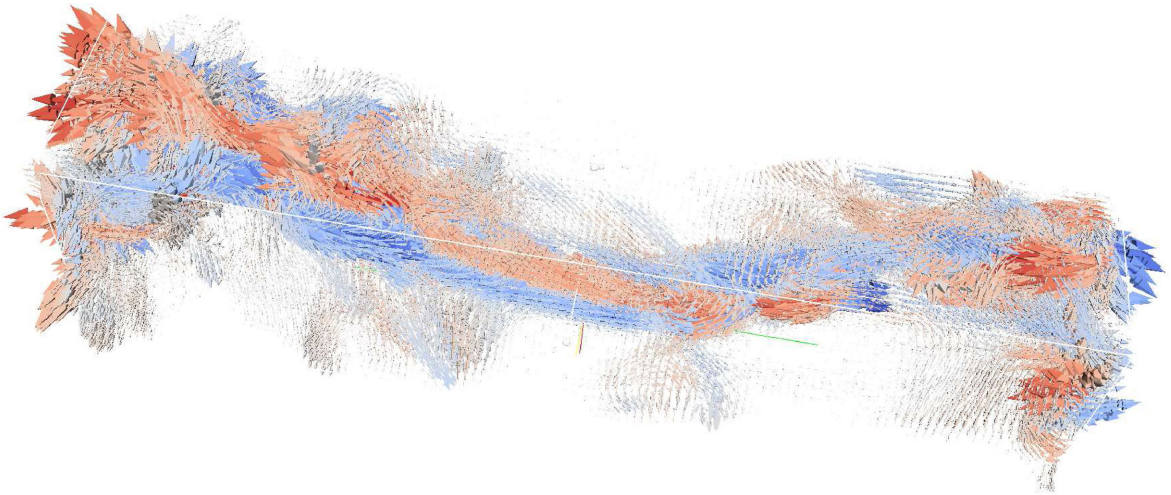

Figure 7. Vorticity field in the neighbourhood of the main filament of the idealized 'HDM' simulation, $\mathcal{S}_{20}^{\rm HDM}$ colour coded through its 'z' component. The vorticity is clearly aligned with the direction of the filament, strongest within its multi-flow core region, while its polarity is twisted around it. Helicity measurements are consistent with the observed level of twisting. We provide animations online at http://www.iap.fr/users/pichon/spin/.

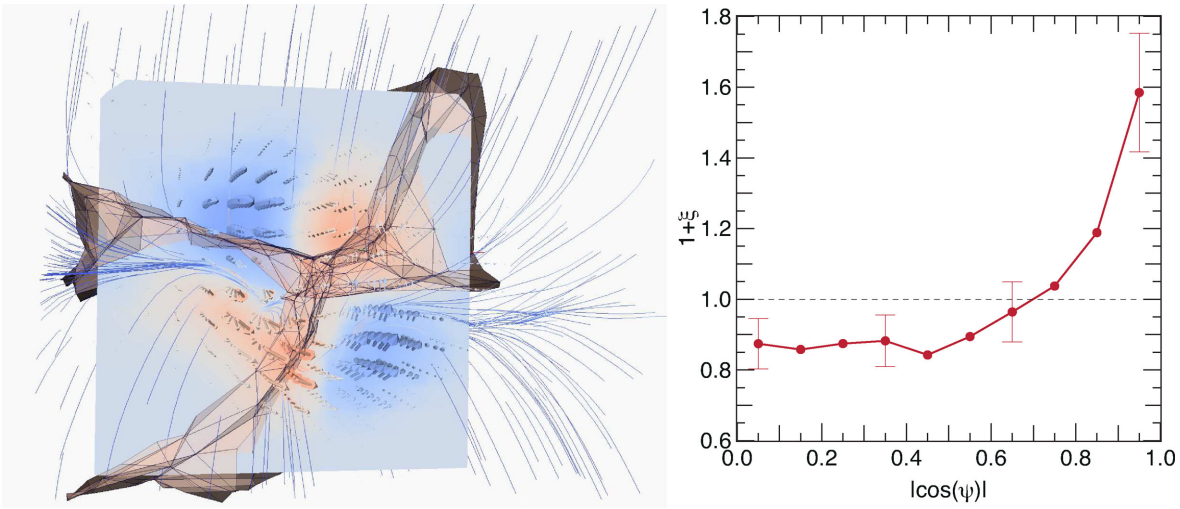

Figure 8. Left: the cross-section of the vorticity perpendicular to the main filament shown in Fig. 7. The colour coding in the section corresponds to the vorticity towards us (in blue) and away from us (in red) as shown by the corresponding arrows. The thin blue lines correspond to velocity field lines. The brown surfaces represent the local walls. The field lines converge towards the local walls and are in agreement with the vorticity field which is partitioned by these walls. Right: the probability distribution as a function of the cosine angle between the normal to the zero vorticity walls and the normal to the density walls, $\cos\psi$, computed on the simulation $\mathcal{S}_{100}^{\rm CDM}$. The simulation is divided into eight 50 h^{-1} Mpc sub-boxes. Density walls are computed using DISPERSE, and the smoothing coefficient of the tessellation is $S = 4$ (see Appendix H). The plotted signal corresponds to the average of the PDFs for the eight sub-boxes. The displayed error bars are 1σ standard deviation on the mean.

This picture is qualitatively consistent with the scenario presented in Codis et al. (2012), as it shows that the filaments are fed via the embedding walls, while the geometry of the flow generates vorticity within their core. This vorticity defines the local environment in which DM haloes form with a spin aligned with that vorticity. The alignment between the contours of minimal vorticity and the density walls which is visually observed in Fig. 8 (left panel) is then quantitatively examined. The probability distribution of the cosine of the angle between the zero vorticity contour and the wall within the caustic is plotted on the right panel of Fig. 8 (see Appendix H for the definition of the zero vorticity contour). An excess of probability of 15 per cent is observed for $\cos\psi$ in [0.5, 1] relative to random distribution, that is for the alignment of the walls with the minimal vorticity contours. This alignment increases with the smoothing of the tessellations, as expected.

4.2 Progenitors of multi-flow region

In a DM (Lagrangian) simulation, it is straightforward to identify the origin of particles within the multi-flow region. Fig. 9 traces back in time DM particles ending up within a quadrant of the multi-flow region. The quadrant is fed by three flows of particles. The flow is irrotational in the initial phase of structure formation until the crossing of three flows in the vicinity of the filaments generates shear and vorticity close to the caustic.

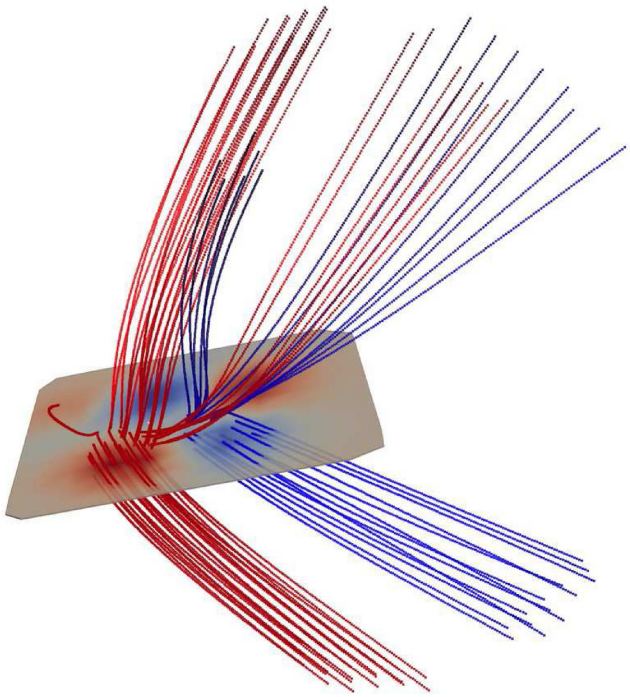

Figure 9. Left: individual DM particle trajectories ending in a given quadrant of the vorticity multi-flow region. In blue are particles ending in a region of positive projected vorticity along the filament, and in red are the particles ending in the negative vorticity region. The quadrant is fed by at least three flows of particles (see also the inset in Fig. 11, which represents qualitatively the theoretical expectation of the starting points of these bundles in the Zel'dovich approximation.). The $\mathcal{S}_{100}^{\rm HDM}$ simulation is used for this figure.

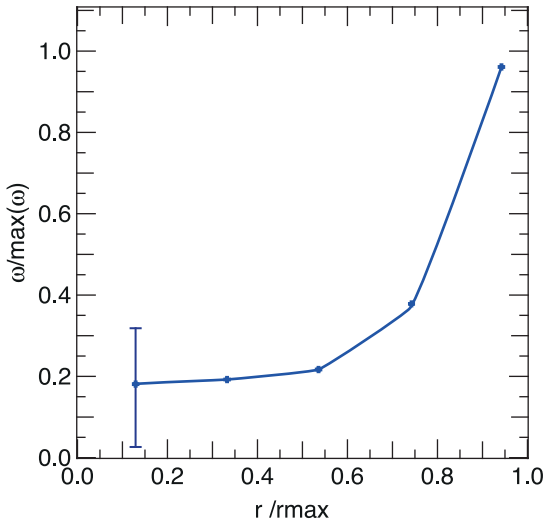

Figure 10. Azimuthal average of the radial profile of the vorticity. The profile is obtained by averaging on the sections of a complete filament (each section is associated with a filament segment, to which the section is perpendicular). Vorticity is clearly larger towards the caustic, and would theoretically become singular (as $1/\sqrt{1-r/r_{\rm max}}$) *at* the caustic for a Zel'dovich mapping, as shown in Pichon & Bernardeau (1999). Here the profile is convolved by shape variations from one caustic to another and by the azimuthal average. The indicative error bar was computed as the average over a larger stack.

Note that the sharp rise near the edge of the multi-flow region at the caustic is qualitatively consistent with catastrophe theory (Arnold 1992), and is directly related to the prediction of Pichon & Bernardeau (1999). Fig. 10 illustrates this fact. To obtain this profile, a filament is cut in slices, corresponding to filament segments: each slice corresponds to a plane perpendicular to the direction of the segment. Local vorticity is measured within that plane and stacked. The amount of vorticity is greater near the caustic. These results are qualitatively consistent with the above-mentioned theoretical predictions which characterize the size and shape of the multi-flow regions after first shell crossing, and estimate their vorticity content as a function of cosmic time.

In short, having looked in detail at the set of (Lagrangian-) smoothed simulations allows us to conclude that streaming motion of DM *away* from minima and wall-saddle points of the field, and *along* the walls of the density field is responsible for generating the multi-flow region in which vorticity arises. In turn, this vorticity defines the environment in which lower mass haloes collapse. Such haloes inherit their spin from this environment, as quantified by Fig. 5.

4.3 Mass transition for spin–filament alignment

Up to now, we have not considered the mass of the forming halo within the multi-flow region. The assumption has been that the Lagrangian extension of the progenitor of the dark halo was small compared to the antecedents of a given vorticity quadrant, so that the collapse occurs within a quadrant of a given polarization, and leads to the formation of haloes with a spin parallel to that vorticity. For more massive objects (of the order of the transition mass), we can anticipate that their progenitor patch overlaps future vorticity quadrants of opposite polarity, hence that they will mostly cancel the component of their vorticity aligned with the filament as they form. The above-mentioned observed transition mass between aligned and anti-aligned spins relative to filaments would then typically correspond to the mass associated with the width of the quadrant of each caustics. In fact, as argued in Pichon & Bernardeau (1999, fig. 7) and shown in Fig. 10, the vorticity within the multi-flow region is mostly distributed near the caustic, on the outer edge of the multi-flow region. It is therefore expected that, as the size of the collapsed halo increases, but remains *below* that of the quadrant, its vorticity should increase (as it collects more and more coherent rotating flow as secondary inflow), as shown in Fig. 5. As it reaches sizes *above* that of the quadrant, it should start to diminish significantly[1] (see also Fig. 11 and Appendix B where this transition is illustrated with the help of a toy model).

Let us turn back specifically to Fig. 6. For the range of mass $\log M/{\rm M}_\odot \approx 11.4$–$12.1$, the alignment between the spin and the direction of the filament *increases* with mass peaking at $M_{\rm max} \approx 10^{12}\,{\rm M}_\odot$, before it rapidly decreases and changes to preferably perpendicular one for $\log M > \log M_{\rm crit} \approx 12.7$, i.e. $M_{\rm crit} \approx 5 \times 10^{12}\,{\rm M}_\odot$. This is fully consistent with the corresponding increase in vorticity shown in Fig. 5.

The characteristic masses can be roughly understood by conjecturing that the highest alignment occurs for the haloes which are of the size of vortices in the caustic regions that *just* undergo collapse. The measured caustic structure depends on the chosen smoothing scale, so a recently formed filament corresponds to the vortex that

[1] In fact, while investigating the statistics of the vorticity within spherical shells, Pichon & Bernardeau (1999) showed that if we consider spheres of size above one quadrant of the multi-flow regions, the total vorticity within that sphere drops significantly.

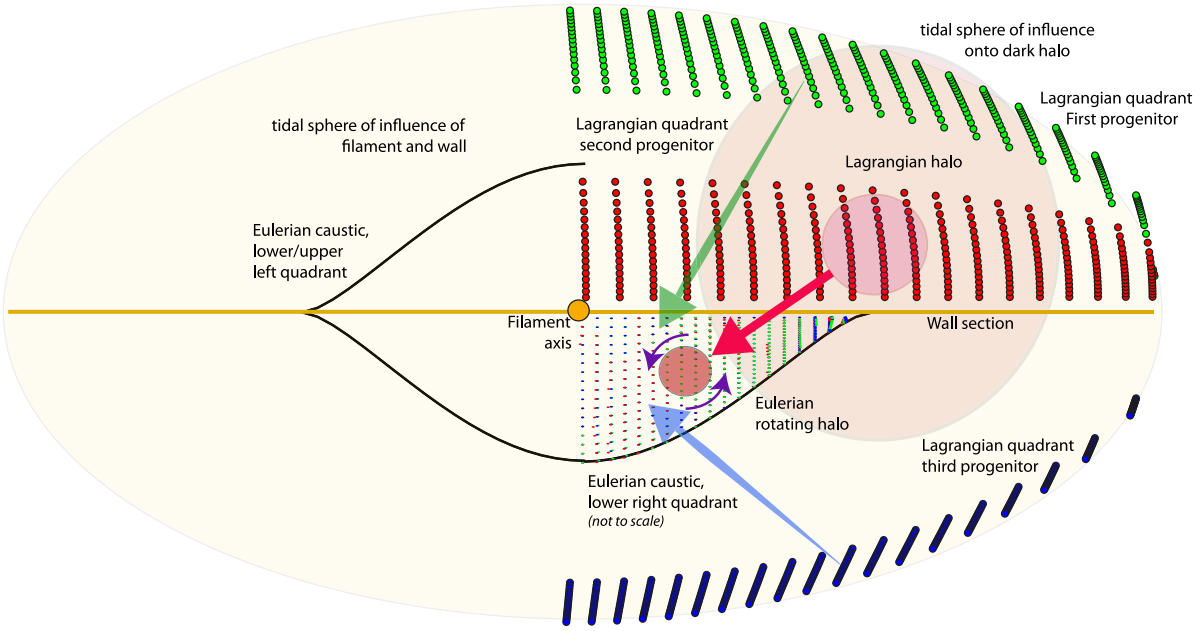

Figure 11. Sketch of the dynamics of a low-mass halo formation and spin-up within a wall near a filament, which are perpendicular to the plane of the image (in yellow). The tidal sphere of influence of this structure is represented by the pale yellow ellipse. The three bundles of large dots (in green, red, and blue) represent Lagrangian points (at high redshift) which image, after shell crossing, will end up sampling regularly the lower right quadrant of the Eulerian multi-flow region; the three progenitor bundles are computed here in the Zel'dovich approximation (see Pichon & Bernardeau 1999, for details; note that this Eulerian quadrant is not up to scale). Each pair of dots (one large, one small) represents the same DM particle in the initial condition and final condition. In black, 3/4 of the Eulerian caustic. In light, resp. dark pink, the locus of the Lagrangian and Eulerian position of the halo, which has moved by a distance displayed by the red arrow, and spun up following the purple arrows while entering the quadrant. The blue and green arrows represent the path of fly-by DM particles originating from the other two bundles, which will contribute to torquing up the halo (following Codis et al. 2012). Given the geometry of the flow imposed by the wall and swirling filament, the spin of the DM halo will necessarily be parallel to the direction of the filament *and* to the vorticity in that quadrant. In the language of TTT, the tidal field imposed on to the Lagrangian patch of the halo (very light pink, corresponding to secondary infall) should be evaluated subject to the constraint that the halo will *move* into the *anisotropic multi-flow* region (each emphasis imposing a constraint of its own); these constraints will in turn impose that the corresponding spin-up will be aligned with the vortex.

shows a basic four quadrant structure and, following Pichon & Bernardeau (1999), which has vorticity close to the Hubble value H. From our simulations, the typical Lagrangian radius of such vortex is $\approx 1.5\,h^{-1}$ Mpc, which if taken as the top-hat scale gives a mass estimate $M_{\rm max} \approx 1.5 \times 10^{12}\,{\rm M}_\odot$ for the mass of haloes with maximum spin/filament alignment. The transition to misalignment will happen at $M_{\rm crit} \approx 8 \times M_{\rm max}$ where the whole width of the filament is encompassed. Of course the quantitative accuracy of such argument should not be over-emphasized. For instance, if we took the Lagrangian radius of the vortex to be $1.3\,h^{-1}$ Mpc, we would get $M_{\rm max} = 10^{12}\,{\rm M}_\odot$, which would fit the transition of Fig. 6 even closer.

5 DISCUSSIONS AND CONCLUSIONS

Let us reframe the findings of Section 3 and 4 in the context of recent published results in this field before concluding.

5.1 Discussion

Libeskind et al. (2013)'s description of AM acquisition occurs in two stages (first through TTT, and then through the curl of the embedding velocity field). Results of Sections 3 and 4 seem consistent with this. In particular the alignment of vorticity with the eigenvectors of the tidal field is confirmed in Appendix E. The connection between Pichon et al. (2011) and this paper is the following: in the former, it was shown that the spin up of dark haloes proceeded in stages: a given collapsing halo would first acquire some specific AM following TTT, at turn around freezing its amplitude at the TTT expected value; in a secondary stage (see their fig. 9), it would spin up again as it acquires specific AM from secondary infall coming from the larger scale distribution of matter which collapses at the next stage of hierarchical clustering. For relatively isolated massive haloes that form from statistically rare density enhancements as studied in Pichon et al. (2011), this secondary collapse just leads to a virialized halo of increased mass. The (Eulerian) emphasis of the current paper and of Codis et al. (2012) (see also Danovich et al. 2011) is to note that for less massive and less rare haloes, forming in large-scale filamentary regions, this secondary infall, coming late from the turn-around of the encompassing filamentary structure, is arriving along marked preferred directions and is typically multi-flow and vorticity rich. Given that the shell crossing occurring during the later formation of that embedding filament generates vorticity predominantly aligned with the filament, this secondary infall will contribute extra spin up along the filament direction. Hence the global geometry of the inflow is consistent with a spin acquisition for haloes induced by the large-scale dynamics within the cosmic web, and in particular its multi-flow vortices. This scenario may only be reconciled with the standard (Lagrangian) tidal torque theory if the latter is augmented so as to account for the larger scale anisotropic environment of walls and filaments responsible for secondary infall (see Pichon et al. 2014).

Let us sketch the basis of such calculation. The geometry of the setting is shown in Fig. 11. For Gaussian random fields, one can

Table 2. The median and mean cosine values for the set of studied alignments. In parenthesis are the expected values for random distributions.

Definition	Name	Mean	Median
Alignment between vorticity and Cosmic Web			
DM: vorticity/filaments		0.58 (0.5)	0.62
Hydro: vorticity/filaments	$\lvert\cos\mu\rvert$	0.58 (0.5)	0.63
DM: vorticity/walls		0.34 (0.5)	0.27
Alignment between vorticity and haloes spin			
$10 \leq \log(M/\mathrm{M}_{\odot}) \leq 11$		0.09 (0.0)	0.14
$10 \leq \log(M/\mathrm{M}_{\odot}) \leq 12$	$\cos\theta$	0.19 (0.0)	0.29
$12 \leq \log(M/\mathrm{M}_{\odot}) \leq 13$		0.53 (0.0)	0.72
Alignment between density walls and 0-vorticity walls			
	$\lvert\cos\psi\rvert$	0.54 (0.5)	0.56
Alignment between vorticity and tidal tensor eigenvectors			
Vorticity/e1		0.62 (0.5)	0.69
Vorticity/e2	$\lvert\cos\gamma\rvert$	0.48 (0.5)	0.47
Vorticity/e3		0.31 (0.5)	0.23

compute the most likely tidal field and inertia tensor at a given Lagrangian peak, subject to a Zel'dovich boost which will translate that peak near to a filament at some distance $\boldsymbol{r}$; this distance corresponds to the time during which the nearby filament has shell-crossed multiplied by the original velocity. In turn, the condition of shell crossing can be expressed as constraints on the eigenvalues of the shear tensor. We can anticipate that the pre-existing Lagrangian correlation between the tidal field of the halo-to-be, on the one hand, and the Hessian of the filament-to-be, on the other hand, imposes some alignment between the direction of the filament (along the first eigenvector of the Hessian) and the spin of the collapsing halo (as set by the corresponding tidal tensor). If the critical condition that the filament is embedded into a given wall is added, the axial symmetry of the problem will be broken, and the inertia and tidal tensor (which are sensitive to different scales) will end up misaligned, reflecting this anisotropy. In this context, the observed spin (and importantly its polarity) will correlate with the polarity of the vorticity quadrant the halo ends up into after translation. The upshot is that in Fig. 11; the lighter pink sphere will 'know' about the green dots given these constraints. This supplementary requirement is imposed by the fact that the correlation between spin and vorticity keeps tract of the direction of both vectors, as shown in Fig. 5. It appears from this sketch that, as the Lagrangian patch of the protohalo becomes of the order of the typical Lagrangian size of the quadrant, the alignment will increase, and as it becomes larger, it will fade (see Appendix B for an illustration of this transition). Note finally that this 'one slice perpendicular to the filament axis' picture cannot address the process of spin flipping to a perpendicular direction to the filament via mergers, as this is a longitudinal process. This is also the topic of Pichon et al. (2014) which complements the Eulerian view presented here.

5.2 Conclusions

Using large-scale cosmological simulations of structure formation, we have analysed the kinematic properties of the velocity flows relative to the cosmic web. Our findings are the following.

(i) The vorticity in large-scale structures on scales of 0.39 h^{-1} Mpc and above is confined to, and aligned with, its filaments with an excess of probability of 20 per cent relative to random orientations, and perpendicular to the normal of the dominant walls at a similar level. This is consistent with the corresponding direction of the eigenvectors of the tidal field (and is expected given that the potential is a smoothed version of the density field).

(ii) At these scales, the cross-sections of these filaments are typically partitioned into quadripolar caustics, with opposite vorticity parallel to their filament, arising from multiple flows originating from neighbouring walls, as would secondary shell crossing along these walls imply. The radial vorticity profile within the multi-flow region displays a sharp rise near the caustic, a qualitatively expected feature of catastrophe theory.

(iii) The spins of embedded haloes within these filaments are consistently aligned with the vorticity of their host vorticity quadrant at a level of 165 per cent. The progenitor of lighter haloes within the multi-flow region can be traced back to three flows or more originating from the neighbouring walls, and form within the filament.

(iv) Appendix A shows that for adiabatic/cooling hydrodynamical simulations within the DM caustics, the gas and the DM share the same vorticity orientation on large scales. High-resolution cooling runs show that the small-scale structure of the velocity flow around forming galaxies does not destroy this larger scale coherence.

(v) The mass transition for spin–filament alignment is set by the size of sub-caustics with a given polarization (see Appendix B). The alignment is strongest for Lagrangian patch commensurable with the sub-caustic as vorticity is strongest on the edge of the multi-flow region. Once the collapsed halo has a size larger than any such sub-caustic, it cancels out most of the vorticity within the caustics.

The focus of this paper was in explaining the 'where': pinning down the locus of vorticity and describing the geometry of multi-flow infall towards filaments; and the 'how': explaining its origin via shell crossing. It also provided an explanation for the origin of the mass transition for spin alignment. All measured alignments are summarized in Table 2.

Improvements beyond the scope of this paper include (i) developing the sketched anisotropic (filamentary) peak-background-split theory of spin acquisition; (ii) quantifying the curvilinear evolution of the vorticity (orientation and amplitude) as a function of distance to the critical points of the cosmic web and predicting the spin flip for high masses; (iii) quantifying the helicoidal nature of gas infall

on galactic scales; (iv) connecting the findings of this paper to the actual process of *galactic* alignment.

In turn, this should allow astronomers to shed light on the following problems: how and when was the present Hubble sequence of galaxies established? How much of the dynamical evolution of galaxies is driven by environment? What physical processes transforming galaxies dominate morphology: galaxy interactions and mergers, external accretion and outflows, secular evolution? What is their respective roles in shaping discs, bulges or spheroids? Is it the same process at low and high redshift? These are addressed in part in the companion paper, Dubois et al. (2014), which shows in particular using state-of-the-art hydrodynamical simulations with AGN/SN feedback that at high redshifts the large vorticity of the gas flow is correlated with the direction of the spin of *galaxies* (their fig. 12).

ACKNOWLEDGEMENTS

We thank M. Haehnelt, James Binney and D. Lynden-Bell for useful comments during the course of this work. JD and AS's research is supported by Adrian Beecroft, the Oxford Martin School and STFC. Let us thank D. Munro for freely distributing his YORICK programming language and OPENGL interface (available at http://yorick.sourceforge.net). Some visualizations made use of the software PARAVIEW http://www.paraview.org. This work is partially supported by the Spin(e) grants ANR-13-BS05-0005 of the French *Agence Nationale de la Recherche* and by the ILP LABEX (under reference ANR-10-LABX-63 and ANR-11-IDEX-0004-02). CP thanks the PEPS 'Physique théorique et ses interfaces' for funding, the institute of Astronomy for a Sacker visiting fellowship and the KITP for hospitality via the National Science Foundation under Grant No. NSF PHY11-25915.

REFERENCES

Aragón-Calvo M. A., Forrest Yang L., 2014, MNRAS, 440, L46
Aragón-Calvo M. A., van de Weygaert R., Jones B. J. T., van der Hulst J. M., 2007, ApJ, 655, L5
Arnold V. I., 1992, Catastrophe Theory/V.I. Arnold [translated from the Russian by G.S. Wassermann; based on a translation by R.K. Thomas, 3rd rev. and expanded edn.]. Springer-Verlag, Berlin, New York
Aubert D., Pichon C., Colombi S., 2004, MNRAS, 352, 376
Bailin J., Steinmetz M., 2005, ApJ, 627
Bett P., Eke V., Frenk C. S., Jenkins A., Helly J., Navarro J., 2007, MNRAS, 376, 215
Birnboim Y., Dekel A., 2003, MNRAS, 345, 349
Codis S., Pichon C., Devriendt J., Slyz A., Pogosyan D., Dubois Y., Sousbie T., 2012, MNRAS, 427, 3320
Danovich M., Dekel A., Hahn O., Teyssier R., 2011, MNRAS, 422, 1732
Doroshkevich A. G., 1970, Astrofizika, 6, 581
Dubois Y., Pichon C., Haehnelt M., Kimm T., Slyz A., Devriendt J., Pogosyan D., 2012, MNRAS, 423, 3616
Dubois Y., Pichon C., Welker C., Le Borgne D., Devriendt J., Laigle C., Codis S., Pogosyan D., 2014, MNRAS, 444, 1453
Haardt F., Madau P., 1996, ApJ, 461, 20
Hahn O., Carollo C. M., Porciani C., Dekel A., 2007, MNRAS, 381, 41
Hoyle F., 1949, Problems of Cosmical Aerodynamics. Central Air Documents, Office, Dayton, OH
Huchra J. P., Geller M. J., 1982, ApJ, 257, 423
Katz N., Keres D., Dave R., Weinberg D. H., 2003, in Rosenberg J. L., Putman M. E., eds, The IGM/Galaxy Connection. The Distribution of Baryons at z=0. Astrophysics and Space Science Library, Vol. 281, How Do Galaxies Get Their Gas? p. 185
Kereš D., Katz N., Weinberg D. H., Davé R., 2005, MNRAS, 363, 2
Kimm T., Devriendt J., Slyz A., Pichon C., Kassin S. A., Dubois Y., 2011, preprint (arXiv:1106.0538)
Libeskind N. I., Hoffman Y., Knebe A., Steinmetz M., Gottlöber S., Metuki O., Yepes G., 2012, MNRAS, 421, L137
Libeskind N. I., Hoffman Y., Forero-Romero J., Gottlöber S., Knebe A., Steinmetz M., Klypin A., 2013, MNRAS, 428, 2489
Libeskind N. I., Hoffman Y., Steinmetz M., Gottlöber S., Knebe A., Hess S., 2013, ApJ, 766, L15
Ocvirk P., Pichon C., Teyssier R., 2008, MNRAS, 390, 1326
Paz D. J., Stasyszyn F., Padilla N. D., 2008, MNRAS, 389, 1127p
Peebles P. J. E., 1969, ApJ, 155, 393
Peirani S., Mohayaee R., de Freitas Pacheco J. A., 2004, MNRAS, 348, 921
Pichon C., Bernardeau F., 1999, A&A, 343, 663
Pichon C., Pogosyan D., Kimm T., Slyz A., Devriendt J., Dubois Y., 2011, MNRAS, 418, 2493
Pichon C., Codis S., Pogosyan D., Dubois Y., Desjacques V., Devriendt J., 2014, preprint (arXiv:1409.2608)
Press W. H., Schechter P., 1974, ApJ, 187, 425
Prieto J., Jimenez R., Haiman Z., 2013, MNRAS, 436, 2301
Pueblas S., Scoccimarro R., 2009, Phys. Rev. D, 80, 043504
Schaefer B. M., 2009, Int. J. Modern Phys. D, 18, 173
Sousbie T., 2011, MNRAS, 414, 350
Sousbie T., Colombi S., Pichon C., 2009, MNRAS, 393, 457
Sousbie T., Pichon C., Kawahara H., 2011, MNRAS, 414, 384
Spergel D. N. et al., 2003, ApJS, 148, 175
Springel V., Yoshida N., White S. D. M., 2001, New Astron., 6, 79
Stewart K. R., Brooks A. M., Bullock J. S., Maller A. H., Diemand J., Wadsley J., Moustakas L. A., 2013, ApJ, 769, 74
Sutherland R. S., Dopita M. A., 1993, ApJS, 88, 253
Tempel E., Stoica R. S., Saar E., 2013, MNRAS, 428, 1827
Teyssier R., 2002, A&A, 385, 337
Teyssier R. et al., 2009, A&A, 497, 335
Tillson H., Devriendt J., Slyz A., Miller L., Pichon C., 2012, preprint (arXiv:1211.3124)
Wang X., Szalay A., Aragón-Calvo M. A., Neyrinck M. C., Eyink G. L., 2014, ApJ, 793, 58
White S. D. M., 1984, ApJ, 286, 38
Zhang Y., Yang X., Faltenbacher A., Springel V., Lin W., Wang H., 2009, ApJ, 706, 747
Zhang Y., Yang X., Wang H., Wang L., Mo H. J., van den Bosch F. C., 2013, ApJ, 779, 160

APPENDIX A: THE VORTICITY OF THE GAS

We use three hydrodynamical simulations $\mathcal{S}_{100}^{\rm HA}$, $\mathcal{S}_{100}^{\rm HC}$ and $\mathcal{S}_{20}^{\rm cool}(0.7)$ (see also Table A1), carried out with the Eulerian hydrodynamic code RAMSES (Teyssier 2002), which uses an Adaptative Mesh Refinement (AMR) technique. For these hydrodynamical runs, the evolution of the gas is followed using a second-order unsplit Godunov scheme for the Euler equations. The HLLC Riemann solver with a first-order MinMod Total Variation Diminishing scheme to

Table A1. The set of hydrodynamical simulations used in Appendix A. The hydro runs come in two categories: adiabatic and cooling, including one high-resolution run which was stopped at redshift 0.7.

Name	Type	Box size h^{-1} Mpc	Resolution
$\mathcal{S}_{100}^{\rm HA}$	ΛHDM adiabatic	100	256^3
$\mathcal{S}_{100}^{\rm HC}$	ΛHDM cool	100	256^3
$\mathcal{S}_{20}^{\rm cool}(0.7)$	ΛCDM cool	20	1024^3

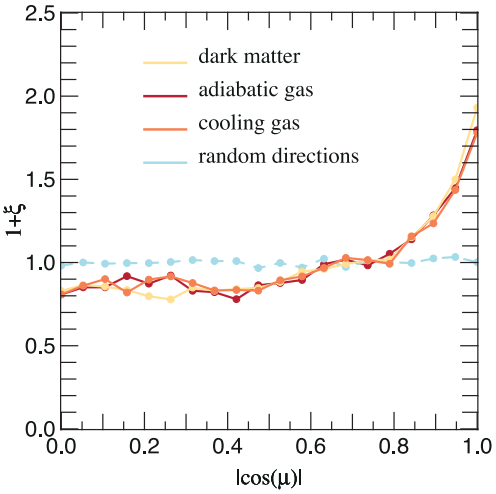

Figure A1. The probability distribution of the cosine of the angle between the vorticity in the smoothed DM and hydrodynamical simulations and the direction of the filament (solid line). The same measure is done for random directions of u (dashed blue line), plotted for the DM in $\mathcal{S}_{100}^{\rm HDM}$ and for the gas in $\mathcal{S}_{100}^{\rm HA}$ (adiabatic gas) and $\mathcal{S}_{100}^{\rm HC}$ (cooling run). We find an excess of probability for $|\cos\mu|$ in [0.5, 1] relative to random orientations, and three profiles are very similar, which shows that large-scale modes dominate.

reconstruct the interpolated variables from their cell-centred values is used to compute fluxes at cell interfaces. Collisionless particles (DM and star particles) are evolved using a particle-mesh solver with a Cloud-In-Cell interpolation. The initial mesh is refined up to $\Delta x = 1.7$ kpc according to a quasi-Lagrangian criterion: if the number of DM particles in a cell is more than eight, or if the total baryonic mass in a cell is eight times the initial DM mass resolution.

For the cooling runs $\mathcal{S}_{100}^{\rm cool}$, and $\mathcal{S}_{20}^{\rm cool}$, gas is allowed to cool by H and He cooling with an eventual contribution from metals using a Sutherland & Dopita (1993) model down to 10^4 K. Heating from a uniform UV background takes place after redshift $z_{\rm reion} = 10$ following Haardt & Madau (1996).

On large scales (as probed by the smoothed sets of simulations) the vorticity of gas shows the same correlations with the filaments as DM does. Fig. A1 displays the probability distribution of the cosine of the angle between the vorticity and the direction of the filament for the DM field (in red), the adiabatic gas (in blue) cooling run (in yellow). These three simulations quantitatively show the same preference for their vorticity to be aligned with the filamentary structure. In a nutshell, differences between the adiabatic and the cooling run only appear on kpc scales, so that on large scales, the DM, adiabatic and cooling runs have the same velocity field structure.

Fig. C1 displays the probability distribution of the cosine of the angle between the vorticity and the direction of the skeleton for a range of redshifts. The correlation between the direction of the filament and the vorticity is significant. As expected, this correlation decreases with cosmic time (at a fixed smoothing scale). Appendix C investigates the evolution of this correlation as a function of the skeleton's persistence. As long as we consider large enough scales, the alignment pervades and is consistent with that of the DM. On smaller scales, the gas is dense enough to allow cooling to operate and re-structure the velocity flow. Notwithstanding, these smaller scale structures do not affect the larger scale correlation between vorticity and the direction of the filaments.

APPENDIX B: TOY MODEL FOR HALO SPIN

Can a model based on a vorticity field in qualitative agreement with what was found in the simulation explain why it should lead the observed evolution of spin alignment with mass? Let us qualitatively illustrate with a simple toy model this mass transition for the spin–filament alignment. In this toy problem, we consider an isolated infinite filament aligned along $\boldsymbol{e}_z$. We define the corresponding idealized vorticity field as

$$\boldsymbol{\Omega}(\boldsymbol{r},\theta) = C\epsilon\,\sin(2\theta)\frac{1}{(\epsilon^2+(r-R)^2)}\,\boldsymbol{e}_z\,,$$

with C a constant, R the radius of the caustic and ϵ a small number. The vorticity thus defined is largest along the caustic, point reflection symmetric and tends rapidly to 0 outside the caustic. Should ϵ tend to 0, vorticity would become singular on the edge of the caustic ($r \to R$). The map of the vorticity is displayed in Fig. B1 (top left panel).

By application of the Helmoltz–Hodge theorem, we find that the curl component of the velocity field consistent with that vorticity (i.e. such that $\boldsymbol{\Omega} = \nabla \times \boldsymbol{v}$) obeys

$$\boldsymbol{v}(\boldsymbol{r},\theta) = \frac{1}{4\pi}\int_{\mathcal{V}} \nabla\times\boldsymbol{\Omega}(\boldsymbol{r}',\theta')\frac{1}{|\boldsymbol{r}-\boldsymbol{r}'|}{\rm d}\mathcal{V}\,. \qquad \text{(B1)}$$

We assume here that the shear part of the curl free component of the velocity flow is smaller on scales comparable to the halo. We now consider a spherical halo of radius $r_{\rm h}$ embedded in one of the four quadrants of the caustic, centred on $C_{\rm h}(x_{\rm h}, y_{\rm h})$ with $x_{\rm h}^2 + y_{\rm h}^2 \leq R$. From equation (B1) we can simply compute its AM $\mathcal{J}(r_{\rm h}, x_{\rm h}, y_{\rm h})$, and look at the variation of $\mathcal{J}$ as a function of its position at fixed radius, or as a function of its radius at fixed position. Fig. B1 (bottom panel) shows the magnitude of the AM along the z-axis for a halo centred on $C_{\rm h}(0.5\,R/\sqrt{2}, 0.5\,R/\sqrt{2})$ as a function of the radius. We observe that the alignment increases until the size of the halo encompasses the whole quadrant. At a given radius, the position of the halo which maximizes the AM is the one for which the edge of the halo coincides with the edge of the caustic, since the vorticity peaks close to the caustic.

APPENDIX C: PERSISTENCE EFFECTS

Given the characteristics of ΛCDM hierarchical clustering, one can anticipate that the process described in the main text occurs on several nested scales at various epochs – and arguably on various scales at the same epoch. The scenario we propose for the origin of vorticity and spin alignment is, like the signal itself, relative to the linear scale involved in defining the filaments and as such multi-scale. Indeed in the main text, the two sets of simulations, $\mathcal{S}^{\Lambda\rm CDM}$ and $\mathcal{S}^{\Lambda\rm HDM}$, allowed us to probe different scales of the vorticity field. The induced multi-scale anisotropic flow also transpires in the scaling of the spin flipping transition mass with smoothing presented in appendix of Codis et al. (2012). It will hold as long as filaments are well defined in order to drive the local cosmic flow.

Let us now briefly explore the effects of probing different scales of the LSS via the skeleton level of persistence. Fig. C1 shows the excess alignment probability as a function of the cosine of the angle between the vorticity and the filaments as a function of the persistence level for a range of values. The alignment is strongest

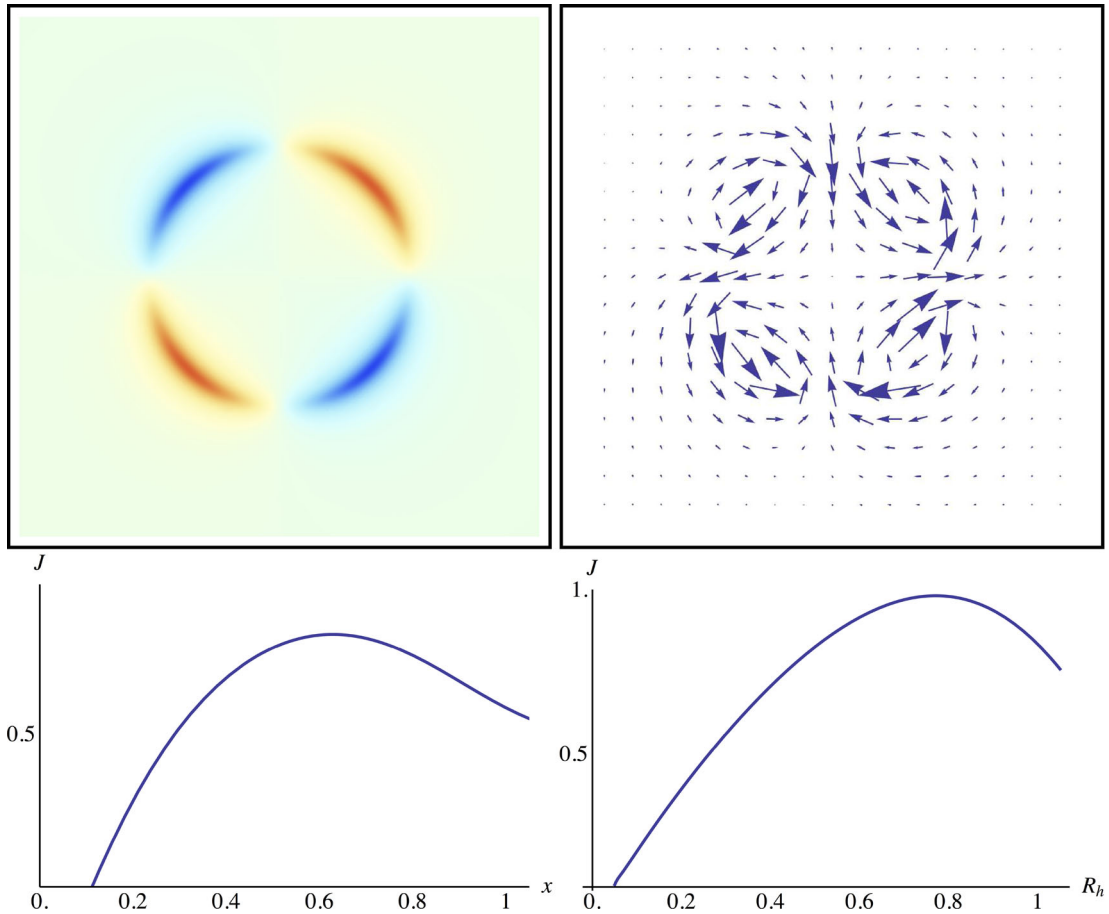

Figure B1. Top: maps of the vorticity (left) projected along $\boldsymbol{e}_z$ and the associated curl component of the velocity (right) computed from the vorticity by application of the Helmoltz–Hodge theorem. Bottom: magnitude of the AM along $\boldsymbol{e}_z$ for a halo embedded in one of the four quadrants. We first consider how it varies as a function of the radius of the halo (left), the position of this latter being fixed $(x_\mathrm{h},y_\mathrm{h}) = (0.5/\sqrt{2}, 0.5/\sqrt{2})$. The alignment of the AM of the halo with the vorticity increases until the halo size becomes comparable to that of the vorticity quadrant. We study then the magnitude of the AM along $\boldsymbol{e}_z$ at fixed radius ($R_\mathrm{h} = 0.3$) as a function of the position x along the diagonal (right). In this case, the alignment increases up to the point where the halo boundary coincides with the vorticity caustic, with the halo still being fully contained within the vorticity quadrant $(x_\mathrm{h},y_\mathrm{h}) \sim (0.7/\sqrt{2}, 0.7/\sqrt{2})$.

with the largest scale filamentary structure corresponding to the least dynamically evolved features of the field. Here the gas density was sampled over a cube of size 512^3. It was then smoothed over 8 pixels (300 kpc) and the persistent skeleton was computed from the logarithm of that smoothed field normalized to its standard deviation. Hence the persistence levels 0.06, 0.12, ..., 2 are in units of this root mean square.

Fig. C2 gives visual impression of the corresponding structure of the skeleton as a function of these persistence levels: the skeleton has a tree-like structure, for which each level of lower persistence contributes smaller branches. Hence the persistence level of 0.5 used in the main text corresponds to a description of the main filaments of the simulation.

APPENDIX D: THE EFFECT OF SMOOTHING

Fig. D1 shows the effect of the smoothing of the velocity field before computing the vorticity on the alignment between the vorticity and the direction of the filament. The amplitude of the excess of alignment varies slightly with the smoothing scale, but the main conclusion that an excess of alignment is detected remains unchanged.

APPENDIX E: TIDAL-VORTICITY LOCKUP

Fig. E1 displays the probability distribution of the cosine of the angle between the vorticity and the eigenvectors of the tidal field tensor, $\cos\gamma$. The vorticity tends to be perpendicular to the minor axis (e_3) of the tidal tensor which corresponds to the axis along which material is collapsing fastest. It is qualitatively in agreement with Fig. 2 and with Libeskind et al. (2013) which focus, respectively, on the eigenvectors of the Hessian of the density, and the eigenvectors of the shear tensor. For the latter, the description is kinematic, rather than dynamical for the tidal field.

APPENDIX F: FOF HALO CATALOGUE

As mentioned in the main text, FOF is prone to spuriously link neighbouring structures which could bias the alignment of the spin and the vorticity. An additional criterion is therefore required to produce a trustworthy catalogue of haloes. Following Bett et al.

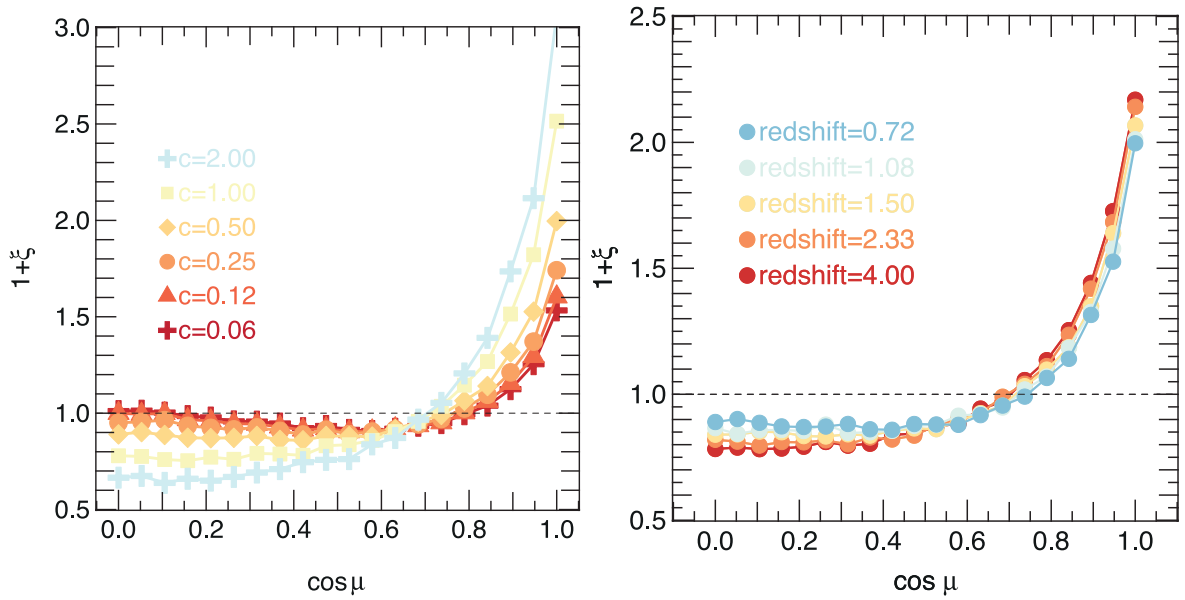

Figure C1. Left: the probability distribution of the cosine of the angle between the vorticity and the direction of the filament measured in $\mathcal{S}_{20}^{\rm cool}(z = 0.7)$ for different persistence threshold. The level of persistence of the main text corresponds to $c = 0.5$. Right: the probability distribution of the cosine of the angle between the vorticity and the direction of the skeleton, measured in $\mathcal{S}_{20}^{\rm cool}(0.7)$ for various redshifts as labelled. The amplitude of the correlation decreases with cosmic time.

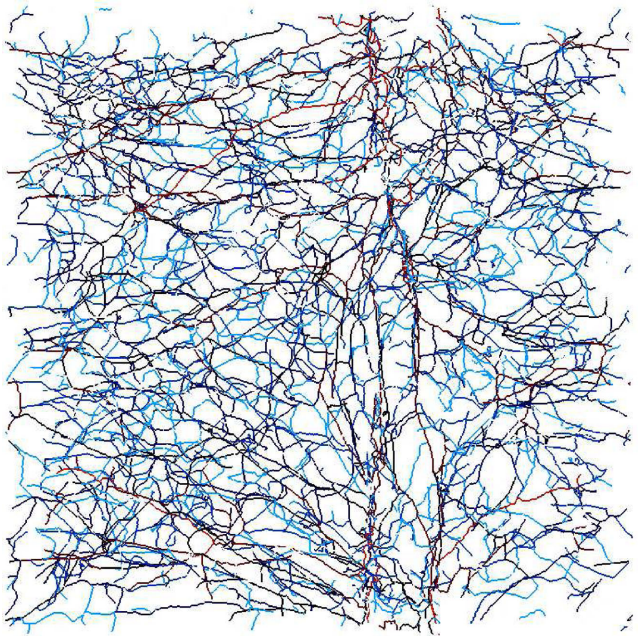

Figure C2. The skeleton measured in $\mathcal{S}_{20}^{\rm cool}(0.7)$ for increasing persistence threshold, 0.06, 0.12,. . . , 2, from light blue to red; the skeleton has tree-like structure where the main branches correspond to the most persistent ones. The level of persistence of the main text corresponds to the dark blue and red branches.

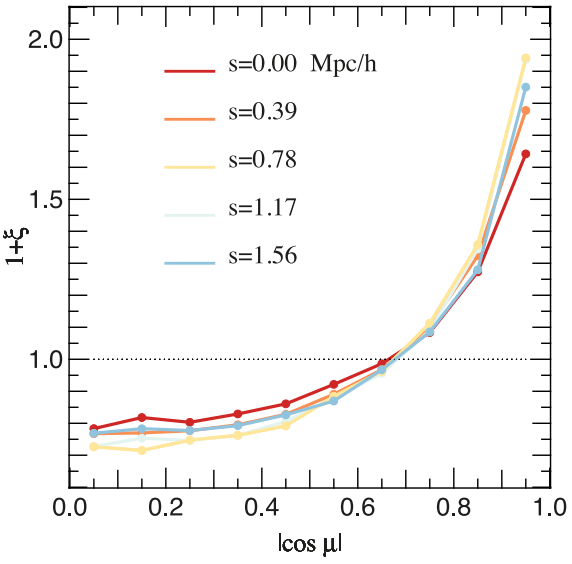

Figure D1. The probability distribution of the cosine of the angle between the vorticity and the direction of the filament, measured in $\mathcal{S}_{100}^{\rm CDM}$ for various smoothing scales of the velocity field before computation of the vorticity. Smoothing scales are expressed in h^{-1} Mpc. The smoothing scale adopted in the main text is 0.39 h^{-1} Mpc.

(2007), we proceed using the distribution of the spin parameter defined by Peebles (1969): $\lambda = J|E|^{1/2}/GM_{\rm h}^{5/2}$, where J is the magnitude of the spin, E is the total energy of the halo, G is the gravitational constant and $M_{\rm h}$ is the halo mass.

Fig. F1 shows the average normalized histogram of the logarithm of the spin parameter for the haloes in the simulations set $\mathcal{S}_{50}^{\rm CDM}$. At high spin we clearly see a long tail, up to $\lambda = 238.2$, due to spurious linking of the structures. We use the analytical model proposed in Bett et al. (2007) to fit the $\log\lambda$-distribution: $P(\log\lambda) = A(\lambda/\lambda_0)^3\exp\left[-\alpha(\lambda/\lambda_0)^{3/\alpha}\right]$, where $A = 3\ln 10\,\alpha^{\alpha-1}/\Gamma(\alpha)$, with the values $\lambda_0 = 0.0341$ and $\alpha = 2.98$ which are providing the best fit. These values are in good agreement

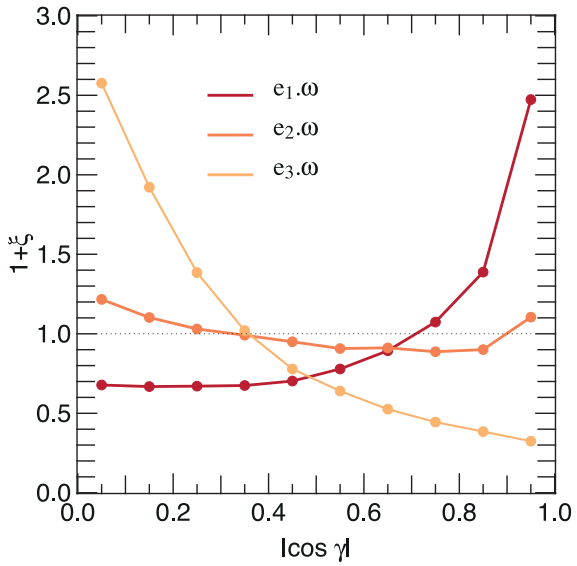

Figure E1. The probability distribution of the cosine of the angle between the vorticity and the eigenvectors of the tidal tensor, measured in $\mathcal{S}_{100}^{\rm CDM}$. The vorticity tends to be perpendicular to the minor axis (e_3) of the tidal tensor: the excess of probability to have $|\cos\theta|$ in [0, 0.5] (i.e. $60 \leq \theta \leq 90^\circ$) is 50 per cent relative to random orientations. The vorticity tends also to be aligned with the major axis (e_1): the excess probability to have $|\cos\theta|$ in [0.5, 1] (i.e. $0 \leq \theta \leq 60^\circ$) is 25 per cent relative to random orientations. e_3 corresponds to the axis along which material is collapsing fastest.

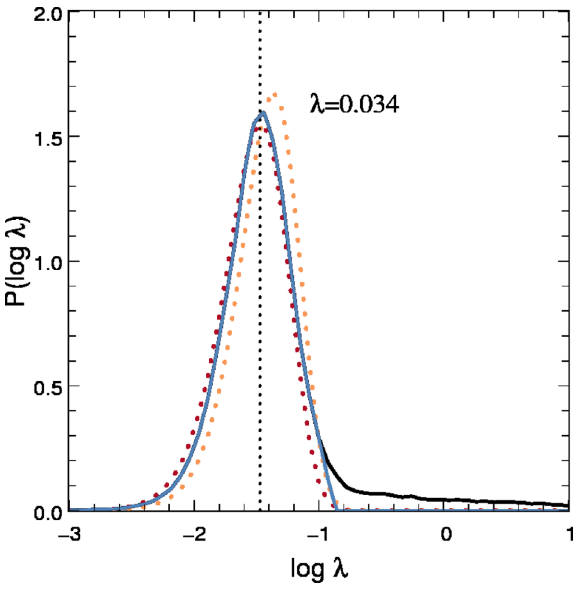

Figure F1. The normalized histogram of the logarithm of the spin parameter in the simulations set $\mathcal{S}_{50}^{\rm CDM}$. The median value of λ is 0.034 ± 0.0005 for the cleaned catalogue. The solid black line is the normalized distribution for all haloes. Notice a tail at high spin parameter which corresponds to spuriously linked structures. The solid blue line is the distribution for haloes with $\lambda \leq 0.12$, with the same normalization as for all haloes. The dotted lines are the analytical fit described in the text, red is our best fit to the distribution, and orange is the best fit found by Bett et al. (2007).

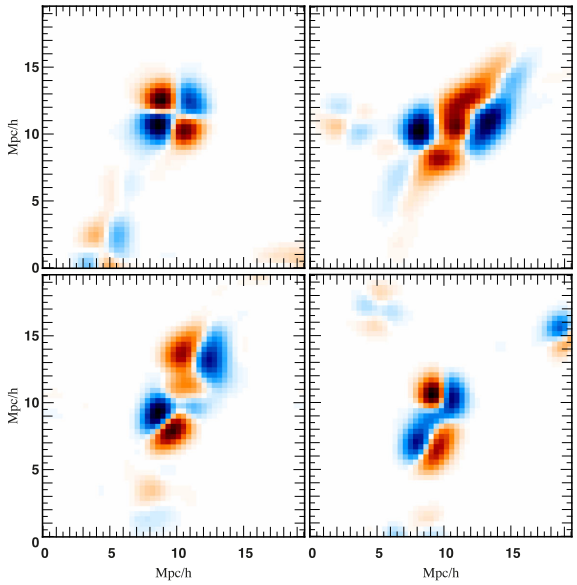

Figure G1. Different kinds of vorticity cross-sections.

with those found by Bett et al. (2007) ($\lambda_0 = 0.043$ and $\alpha = 2.51$), though their way to clean their catalogue (TREEall) is more sophisticated, in particular by taking into account an additional condition on energy. They showed also that the minimal number of particles per halo, $N_{\rm p}$, clearly affects the λ-distribution only for $N_{\rm p}$ lower than 100. Above this threshold, the change in the median value of λ stays lower than 10 per cent. Consequently, we keep in our catalogue only haloes with more than 100 particles. These haloes are then selected through a cut in λ. We find that removing haloes with $\lambda \geq 0.12$ best fits the adopted analytical model. Removed haloes represent 9.4 ± 1.2 per cent of the total population. Inspection of some of these removed haloes shows that they generally are multiple objects. We are left with around 5000 haloes in each $50\,h^{-1}$ Mpc box of the $\mathcal{S}_{50}^{\rm CDM}$ simulations set.

We then quantify how the cut in λ affects the vorticity–spin alignment results. Considering three different catalogues with three different cuts in λ ($\lambda < 0.08$, $\lambda < 0.12$, $\lambda < 0.2$) we look for each catalogue and for each bin of mass at the quantity $(\zeta_{\rm tot} - \zeta_{\rm cut})/(1 + \zeta_{\rm tot})$ where $1 + \zeta_{\rm cut}$ is the excess of alignment in the reduced catalogue and $1 + \zeta_{\rm tot}$ in the full catalogue. This difference is always <5 per cent. We conclude that including or not the misidentified structures does not significantly change the measure of the spin alignment with the vorticity.

APPENDIX G: ZOOLOGY OF CAUSTICS

Fig. G1 shows a bundle of cross-sections of vorticity computed as in Fig. 3.

APPENDIX H: DEFINING ZERO VORTICITY

The algorithm DISPERSE introduced by Sousbie (2011) is used to defined the density walls and the contours of minimal vorticity. The density walls are computed as being the ascending two–manifolds of the skeleton calculated on the density field. The contours of minimal vorticity are defined as being the descending two–manifolds of the skeleton calculated on the norm of the vorticity

field. Since the vorticity is really well defined only on the neighbourhood of caustics, a mask is applied when the walls are computed, which covers all the regions of space where the density is lower than 10 per cent of the maximum density and the vorticity lower than 10 per cent of the maximum vorticity. The results of the computation of the density walls and minimal vorticity contours are tessellations, which means sets of triangles. For each triangle in the minimal vorticity tessellation we find its nearest neighbours in the density tessellation. Smoothing is achieved by averaging the position of each vertex with that of its direct neighbours. A smoothing coefficient $S = N$ means that this operation is repeated N times. The cosine between the normals of both triangles is then calculated.

This paper has been typeset from a TEX/LATEX file prepared by the author.